arXiv:2112.06118v1 [astro-ph.SR] 12 Dec 2021

Simultaneous Observations of Chromospheric Evaporation and Condensation during a C-class Flare

Dong Li[1,2,3], Zhenxiang Hong[1,2], and Zongjun Ning[1,2]

[1]*Key Laboratory of Dark Matter and Space Astronomy, Purple Mountain Observatory, CAS, Nanjing 210023, PR China*

[2]*School of Astronomy and Space Science, University of Science and Technology of China, Hefei 230026, PR China*

[3]*CAS Key Laboratory of Solar Activity, National Astronomical Observatories, Beijing 100101, PR China*

ABSTRACT

We explored simultaneous observations of chromospheric evaporation and condensation during the impulsive phase of a C6.7 flare on 9 May 2019. The solar flare was simultaneously observed by multiple instruments, i.e., the New Vacuum Solar Telescope (NVST), the Interface Region Imaging Spectrograph, the Atmospheric Imaging Assembly (AIA), the Fermi, the Mingantu Spectral Radioheliograph, and the Nobeyama Radio Polarimeters. Using the single Gaussian fitting and the moment analysis technique, redshifted velocities at slow speeds of 15−19 km s^{-1} are found in the cool lines of C II and Si IV at one flare footpoint location. Red shifts are also seen in the Hα line-of-sight (LOS) velocity image measured by the NVST at double footpoints. Those red shifts with slow speeds can be regarded as the low-velocity downflows driven by the chromospheric condensation. Meanwhile, the converging motions from double footpoints to the loop top are found in the high-temperature EUV images, such as AIA 131 Å, 94 Å, and 335 Å. Their apparent speeds are estimated to be roughly 126−210 km s^{-1}, which could be regarded as the high-velocity upflows caused by the chromospheric evaporation. The nonthermal energy flux is estimated to be about 5.7×10^{10} erg s^{-1} cm^{-2}. The characteristic timescale is roughly equal to 1 minute. All these observational results suggest an explosive chromospheric evaporation during the flare impulsive phase. While a HXR/microwave pulse and a type III radio burst are found simultaneously, indicating that the explosive chromospheric evaporation is driven by the nonthermal electron.

Subject headings: Solar flares — Solar chromosphere — Solar ultraviolet emission — Solar X-ray emission — Solar radio emission — line profiles

Correspondence should be sent to: lidong@pmo.ac.cn

1. Introduction

Solar flare generally shows a sudden brightening feature on the Sun, which is often accompanied by a quick and violent energy release via magnetic reconnection (e.g., Fletcher et al. 2011; Benz 2017; Chen et al. 2020; Tan et al. 2020). The wavelength range of flare radiation is quite broad, i.e., from the radio/microwave through the white light and extreme ultraviolet (UV/EUV) to soft/hard X-rays (SXR/HXR) and even to the γ-ray (e.g., Masuda et al. 1994; Su et al. 2013; Dominique et al. 2018; Yan et al. 2018a,b; Lysenko et al. 2020; Li et al. 2021). In the standard model of a solar flare such as the CSHKP flare model (Carmichael 1964; Sturrock 1966; Hirayama 1974; Kopp & Pneuman 1976), a huge amount of magnetic energies are released via reconnection in the local corona (Shibata & Magara 2011; Li et al. 2016; Jiang et al. 2021), i.e., as described in the two-dimensional reconnection model (Sturrock & Coppi 1964; Priest & Forbes 2002; Lin et al. 2005). In the reconnection site, the local plasma will be heated to the thermal energy, while the electron will be accelerated to the nonthermal energy. Subsequently, some accelerated electrons could travel upward along the open magnetic lines and escape away or may propagate upward along the closed magnetic field lines, while the other electron beams will transport downward along the closed magnetic lines, and then precipitate in the chromosphere. This has been known as 'bi-directional outflows' (e.g., Innes et al. 1997; Mann & Warmuth 2011; Liu et al. 2013; Li 2019; Warmuth & Mann 2020; Yan et al. 2021a). In the chromosphere, the precipitated electrons could heat the localized plasma rapidly up to a very high temperature via coulomb collisions, resulting overpressure in the localized chromosphere. The overpressure can drive the chromospheric material upward along the new formed flare loop into the overlying corona at a fast speed, for instance, an order magnitude of hundreds of km s^{-1}. The hot material fills up the newly flare loop rapidly in a process regarded as 'chromospheric evaporation' (e.g., Fisher et al. 1985; Teriaca et al. 2003; Brosius & Daw 2015; Dudík et al. 2016; Tian & Chen 2018). In this process, double footpoints at the loop legs are often generated in the HXR or microwave emissions, and the flare ribbons could be seen in Hα, white light, UV or low-temperature EUV wavelengths, while flare loops can be found in the SXR and high-temperature EUV images (e.g., Sui & Holman 2003; Asai et al. 2006; Temmer et al. 2007; Krucker et al. 2008; Brosius et al. 2016; Chen et al. 2017; Song et al. 2018). Due to the momentum conservation, the overpressure of the chromosphere can simultaneously cause downward mass motions into the underlying chromosphere at a slow speed, a process termed 'chromospheric condensation' (Kamio et al. 2005; Zhang et al. 2016a; Libbrecht et al. 2019; Graham et al. 2020; Yu et al. 2020).

Observations of the chromospheric evaporation have been widely reported in the flare radiation at wavelengths of radio, UV/EUV, and HXR. In the radio dynamic spectrum, the higher frequency suddenly being suppressed and drifting to lower frequencies can be regarded as the radio evidence of chromospheric evaporation (Aschwanden & Benz 1995; Karlicky 1998; Ning et al. 2009). In the HXR images, the HXR emissions often appear firstly at two footpoint sources, and then rise upward along their loop legs, subsequently merge into a single source at the loop-top region (Liu et al. 2006, 2008; Ning & Cao 2010, 2011; Ning 2011). The same observational features can also be

seen in the high-temperature EUV images, for instance, the drastic mass motions from the double footpoints along the hot flare loop to the loop top (Li et al. 2017; Zhang et al. 2019). This is regarded as the HXR/EUV signature of chromospheric evaporation (e.g., Liu et al. 2006; Ning 2011; Zhang et al. 2019). The mergence/move speed could be as high as about 200 km s^{-1}, which is roughly equal to the upflow speed of the hot evaporated materials. Thanks to the spectroscopic observations, the chromospheric evaporation in solar flares can be well diagnosed by the line profile (e.g., Milligan & Dennis 2009; Doschek et al. 2013; Tian et al. 2014; Li et al. 2015; Polito et al. 2017; De Pontieu et al. 2021). In the typical chromospheric evaporation, the hot coronal lines always appear high-velocity blue shifts, which are attributed to the fast upward mass motions. While the cool chromospheric or transition region lines could exhibit low-velocity red shifts due to the slow downward mass motions, or may show blue shifts without associated clear downflows. The former one is often regarded as 'explosive evaporation' (Milligan et al. 2006a; Zhang et al. 2016b; Brosius & Inglis 2017; Li et al. 2017), and the latter one is referred as 'gentle evaporation' (Milligan et al. 2006b; Sadykov et al. 2015; Li et al. 2019). These two types of chromospheric evaporation are often depending on the heating energy of electron beams, for instance, a critical threshold of about 10^{10} erg s^{-1} cm^{-2} (e.g., Fisher et al. 1985; Kleint et al. 2016; Sadykov et al. 2019). However, the threshold value of the deposited energy flux is not a constant, it is sensitive to the duration of the heating and the location of the energy deposition (Reep et al. 2015; Polito et al. 2018). Rubio da Costa et al. (2015) stated that the explosive evaporation could also be caused by stochastic accelerated electrons with a low energy flux that is less than 10^{10} erg s^{-1} cm^{-2}.

Chromospheric evaporation has been detected in a large number of solar flares (e.g., Ding et al. 1996; Li & Ding 2004; Falewicz et al. 2009; Raftery et al. 2009; Chen & Ding 2010; Veronig et al. 2010; Li & Ding 2011; Brosius 2013; Young et al. 2015; Brosius & Inglis 2018; Tian & Chen 2018), largely benefiting from the spectroscopic observations, such as, the Bragg Crystal Spectrometer on board Yohkoh, the Coronal Diagnostic Spectrometer aboard the Solar and Heliospheric Observatory, the Extreme-ultraviolet Imaging Spectrometer experiment aboard Hinode, the Interface Region Imaging Spectrograph (IRIS), et cetera. They can be detected in the pre-flare phase (Brosius & Holman 2010; Li et al. 2018), impulsive phase (Graham & Cauzzi 2015; Li et al. 2017; Sadykov et al. 2019) and gradual/decay phase of solar flares (Czaykowska et al. 1999; Li et al. 2012; Brannon 2016). The chromospheric evaporation could be explained by the electron driven (Tian et al. 2015; Warren et al. 2016; Lee et al. 2017) or the thermal conduction driven (Czaykowska et al. 2001; Battaglia et al. 2015; Ashfield & Longcope 2021), as well as the dissipation of Alvén waves (Fletcher & Hudson 2008; Reep & Russell 2016). The first one states that the nonthermal energy produced by electron beams plays an important role in the evaporation process, while the second one emphasizes that the evaporation motion is directly driven by the thermal energy. In this paper, we present observational evidences of an explosive chromospheric evaporation during the impulsive phase of a solar flare, and it appears to be driven by the nonthermal electron.

2. Observations and Instruments

A solar flare occurred on 9 May 2019 in active region (AR) NOAA 12740, which was close to the solar disk center, e.g., N09E13. Based on the solar monitor[1], the flare was a C6.7 class, and it started at about 05:40 UT, reached its maximum at around 05:51 UT. It was simultaneously measured by the IRIS (De Pontieu et al. 2014), the New Vacuum Solar Telescope (NVST, Liu et al. 2014), the Atmospheric Imaging Assembly (AIA, Lemen et al. 2012) and the Helioseismic and Magnetic Imager (HMI, Schou et al. 2012) for the Solar Dynamics Observatory (SDO, Pesnell et al. 2012), the X-ray Telescope (XRT, Golub et al. 2007) of the Hinode mission, as well as the Geostationary Operational Environmental Satellite (GOES-16, Loto'aniu et al. 2017), the Fermi Gamma Ray Burst Monitor (GBM, Meegan et al. 2009), the Mingantu Spectral Radioheliograph (MUSER, Yan et al. 2021b), and the Nobeyama Radio Polarimeters (NoRP, Nakajima et al. 1985), as listed in table 1.

The NVST is a one meter aperture vacuum telescope located at Fuxian Solar Observatory, which is operated by Yunnan Observatories. It can provide high-resolution images of the chromosphere and photosphere, corresponding to the channels of Hα and TiO, respectively (Liu et al. 2014; Yan et al. 2020a). In this paper, the NVST Hα images at the line core (6562.8 Å) and two off bands ($\pm$0.5 Å) are acquired from 05:35 UT to 09:58 UT on 9 May 2019. Using the speckle masking method (Weigelt 1977; Lohmann et al. 1983; Xiang et al. 2016), these images are reconstructed from the Level 1 to Level 1+, which can be accessed at the NVST website[2]. They have a spatial pixel size of $\sim$0.165″ and a time cadence of $\sim$43 s.

The IRIS provides multi-channel UV imaging spectrograph in space, which is mainly focused on the solar chromosphere and transition region (De Pontieu et al. 2014). On 9 May 2019, IRIS scanned the AR NOAA 12740 in a 'very large dense 320-step raster' mode, which had a max field-of-view (FOV) of $\sim$279″ $\times$175″. The step size and cadence were 0.35″ and $\sim$16.2 s, respectively, while the pixel scale along the slit was $\sim$0.33″. The far UV (FUV) spectra and images are acquired from the IRIS level 2 data, which has been pre-processed and calibrated by the IRIS team. Here, we used the spectral lines at spectral windows of 'Si IV 1394 Å', 'Si IV 1403 Å', and 'C II 1336 Å', as well as the Slit-Jaw Imager (SJI) at 1400 Å. The FUV spectra has a spectral dispersion of about 0.0256 Å pixel^{-1}, and the SJI 1400 Å images had a time cadence of $\sim$65 s.

The SDO/AIA is designed to take full-disk solar images in multiple wavelengths nearly simultaneously (Lemen et al. 2012), and the SDO/HMI is designed to investigate the solar magnetic field and oscillatory features on the Sun (Schou et al. 2012). Here, the AIA images at high-temperature EUV wavelengths of 131 Å ($\sim$10 MK), 94 Å ($\sim$6 MK), and 335 Å ($\sim$3 MK) are used, which have a time cadence of 12 s. We also used the HMI line-of-sight (LOS) magnetogram to show the distribution of magnetic fields. Both the AIA EUV images and the HMI LOS magnetogram have been

[1]https://www.lmsal.com/solarsoft/latest_events_archive/events_summary/2019/05/09/gev_20190509_0540/index.html

[2]http://fso.ynao.ac.cn/cn/datashow.aspx?id=2344

pre-processed via the AIA and HMI standard routines, such as 'aia_prep.pro' and 'hmi_prep.pro'. Then, they both have a spatial scale of 0.6″ pixel^{-1}. The Hinode/XRT provides solar images via nine X-ray filters, which measures the coronal plasma from about 1 MK to approximately 20 MK, and they were calibrated using the standard XRT program such as 'xrt_prep.pro' before analyzing (Golub et al. 2007). During the C6.7 flare, the XRT takes synoptic data in the form of full-disk images with both long and short exposures from 05:40:03 UT to 05:43:49 UT, and the spatial scale is ∼4.1″ pixel^{-1}.

The C6.7 flare was also recorded by the MUSER, NoRP, Fermi/GBM, and GOES at radio, HXR and SXR emissions. The MUSER could provide the radio dynamic spectrum between 0.4 GHz and 2.0 GHz. It has forty 4.5-m reflector antennas distributed in three spiral arms, which can measure dual circular polarizations with a time resolution of 0.025 s (Yan et al. 2009, 2021b). The NoRP and the Fermi/GBM observed the entire Sun with multiple channels in microwave and X-ray ranges, respectively. In this study, we used the radio dynamic spectrum detected by the No.33 antenna of MUSER, because we did not find any pronounced polarization in the radio bursts for the forty antennas during the observed time. The microwave flux at the frequency of 3.75 GHz with a time cadence of 1 s was used (Nakajima et al. 1985). The HXR flux at 26.6−50.4 keV recorded by the n3 detector was used, which has a time resolution of about 4.096 s (Meegan et al. 2009). Noting that the HXR light curve was derived from the cspec file rather than the ctime file, because we also perform the X-ray spectral analysis to look the deposited energy flux. The SXR flux at 1−8 Å recorded by the GOES-16 was also used, which has a time cadence of 1 s.

3. Data analysis and Results

Figure 1 presents the overview of the solar flare on 9 May 2019. Panel (a) plots the SXR 1−8 Å light curve recorded by the GOES-16, which suggests that the flare peak flux could exceed 10^{-5} Watts m^{-2}. It should be pointed out that the GOES XRS flux has been corrected by a constant factor of about 1.5 for above the C1-class flare (Woods et al. 2017). However, it was regarded as a C6.7 class flare in the solar monitor, which was from the GOES-14 SXR flux. In this paper, we also regard it as a C6.7 class, which is similar to the previous study (Yan et al. 2020b). It began at about 05:40 UT, and peaked at roughly 05:51 UT. The HXR and microwave fluxes recorded by the Fermi/GBM and NoRP are also presented in Figure 1 (a). They both show three main pulses ('1'−'3') during ∼05:43−05:49 UT, which is in the impulsive phase of the C6.7 flare and could be regarded as the quasi-periodic pulsations (Hong et al. 2021). In panel (b), three groups of transient bursts can be seen in the radio dynamic spectrum measured by the MUSER during the same time interval, and they drift rapidly from the high frequency to the low frequency over a very short time. Thus, they could be regarded as three groups of type III radio bursts, revealing a well one-to-one correspondence with the three HXR/microwave pulses, as indicated by the Roman numerals in Figure 1 (a) and (b). All these observations imply that pulsed nonthermal electrons are intermittently accelerated by the repeated magnetic recognition during the flare impulsive phase.

In Figure 2, we show the multi-wavelength snapshots of the C6.7 flare with the same FOV of about $130''\times130''$. Panels (a) and (b) present high-temperature coronal images at nearly the same time during the solar flare, i.e., XRT Al_mesh, and AIA 131 Å. They both show a bright loop-like structure, as outlined by the purple contour. Thus, the XRT and AIA images can be co-aligned with the cross-correlation method. The loop-like structure observed in the high-temperature coronal images could be regarded as a potential candidate of the hot flare loop, as indicated by the purple arrow. Here, the XRT Al_mesh image is selected because it corresponds pixels in the short exposure that are not saturated. Panels (c) & (d) present the SJI 1400 Å and Hα 6562.8 Å images measured by the IRIS and NVST. The bright and strip features can be simultaneously seen in the SJI 1400 Å and Hα line-core images, which might be regarded as the flare ribbons, as indicated by the cyan arrows. Moreover, one of the flare ribbons was crossed by the IRIS slit, as indicated by the dashed vertical line in panel (c). Panels (e) & (f) plot the NVST images in two Hα off bands at ±0.5 Å, and they are used to obtain the LOS velocity image. The NVST and IRIS data can be co-aligned by using the cross-correlation technique, because they both show the bright flare ribbons. While the AIA 1600 Å image (panel g) is applied to co-align with the SJI 1400 Å image, since they both contain the continuum emissions from the temperature minimum (see, Li et al. 2015; Tian et al. 2015). Panels (h) & (i) show the AIA 94 Å running difference map and the HMI LOS magnetogram. A bright loop-like structure appears in the AIA 94 Å running difference map. To clearly see the bright loop, we plot the AIA 94 Å running difference map with a small FOV of about $30''\times30''$, as shown by the zoomed image in panel (h). It is very similar to the high-temperature images in AIA 131 Å and XRT/Al_mesh. Moreover, the two-end locations of the loop-like structure are rooted in the positive (Ft1) and negative (Ft2) magnetic fields, respectively, as indicated by the cyan curve in panel (i). In panel (h), the overplotted contours represent the AIA 94 Å emissions at three fixed instances of time. They begin to brighten in two separated locations, for instance, the two red contours at about 05:43:35 UT. Then they move closely along the loop-like structure, as indicated by the two blue contours at about 05:43:59 UT. At about 05:44:35 UT, only one bright source (yellow) can be seen, which can be regarded as the loop-top source. All these observational facts confirm the bright loop-like structure could be regarded as the hot flare loop, and the two brightening locations can be regarded as the double footpoints (Ft1 and Ft2) connected by the flare loop. Yan et al. (2020b) suggested that the AR NOAA 12740 was made up of a large compact leading negative polarity and some small diffuse positive following polarities. The C6.7 flare took place at the northeast edge of the leading negative magnetic field, as shown in panels (c)−(i). An AR filament located at the northeast of the leading sunspot can be seen in the Hα image (panel d), and it was a failed filament eruption (see detail, Yan et al. 2020b).

One slit of the IRIS crossed the flare ribbon, which is well used to study the chromospheric evaporation (e.g., Li et al. 2015; Tian et al. 2015; Young et al. 2015; Polito et al. 2017; Li et al. 2018; Graham et al. 2020). We then plot the IRIS spectra at three FUV windows of 'Si IV 1394 Å', 'Si IV 1403 Å', and 'C II 1336 Å', as shown in Figure 3 (a)−(c). Panel (d) draws the LOS velocity image obtained by the two off-bands (±0.5 Å) Hα images at almost the same time. Thus, it is only a qualitative description rather than the quantitative calculation. The interested site is marked by

the solid green line, which is regarded as one footpoint (Ft2) of the hot flare loop, and it appears a weak redshifted velocity. The other footpoint (Ft1) also exhibits weak redshifted velocities in the Hα LOS velocity image, as indicated by the cyan arrow. But we cannot check the IRIS spectra at the other footpoint, because it was not crossed by the IRIS slit during the C6.7 flare. We notice that both IRIS spectral lines and Hα LOS velocity image shown strong blueshifted velocity at Y$\sim$200$-$220$''$ along the IRIS slit, and then become strong redshifted velocity at Y$\sim$180$-$200$''$. However, they are out of the scope of this study., because they are far away from the hot flare loop, as shown in Figure 2. The line spectra at the quiet region (outlined by the dashed green lines) are also selected to determine their rest wavelengths or reference line centers, as indicated by the vertical pink lines.

To look closely the Doppler velocity, we then extract the spectral line profiles from the IRIS spectra at the footpoint (Ft2) location nearby the flare ribbon, as shown in Figure 4. Panels (a) & (b) plot the line spectral profiles at IRIS FUV windows of 'Si IV 1394 Å' and 'Si IV 1403 Å', containing the transition region lines of Si IV , which are widely applied to study the chromospheric condensation (e.g., Battaglia et al. 2015; Brannon 2016; Brosius & Inglis 2017; Li et al. 2017; Tian & Chen 2018; Yu et al. 2020). Similar to previous findings (Zhang et al. 2016b; Li et al. 2018, 2019), each line spectrum is isolated, showing a good Gaussian profile at the site of the flare footpoint. Therefore, each observed line profile of Si IV is fitted by a single Gaussian function superimposed on a constant background. The fitting result for each line profile is overplotted with a magenta curve, which corresponds well with the raw line profile. Panel (c) presents the line spectral profile at 'C II 1336 Å' window, which contains the double C II lines formed in the lower transition region. It can be seen that they appear central-reversed line profiles. Thus, the moment analysis (e.g., Li et al. 2019; Yu et al. 2020) rather than the Gaussian fitting is applied to the observed C II line profile. The Doppler velocity of each spectral line is determined by its real line center subtracting the rest wavelength. The real line centers of Si IV and C II lines are identified from the single Gaussian fitting and moment analysis method, respectively. The rest wavelengths are determined from their line profiles in the quiet region. To improve the signal-to-noise ratio, the line profile in the quiet region is averaged over 10 pixels between about Y$\approx$172.1$''$ and Y$\approx$175.4$''$ along the IRIS slit, as outlined by the two dashed green lines in Figure 3. It should be pointed out that the line profiles in the quiet region are multiplied by 10, so that they can be clearly seen in the same window with the flare footpoint line spectra. Their Doppler velocities are easy to be estimated from their line centers and rest wavelengths, which are roughly equal to 18 km s^{-1} for the Si IV lines and 17 km s^{-1} for the C II lines, as given in Figure 4. In order to provide the spectral information at the different footpoint locations, we plot three other IRIS line spectra at the window of 'Si IV 1394 Å' before and after 05:44:15 UT, as shown in Figure 5 (b)$-$(d). Their slit positions are marked by the solid vertical lines in panel (a), which shows the zoomed LOS velocity image in the Hα waveband. Similar to previous results, each observed line profiles (black) is isolated, revealing a good Gaussian profile. Therefore, it is fitted with a single Gaussian function superimposed on a constant background, as indicated by the overplotted magenta curve in each panel. The Doppler velocities are estimated to be about 15$-$19 km s^{-1}, and they all show red-shifted velocities.

The red shifts of cool lines at the flare footpoint locations could be regarded as downflows caused by the chromospheric condensation (e.g., Zhang et al. 2016a; Libbrecht et al. 2019; Graham et al. 2020; Yu et al. 2020). However, we could not find blue shifts of the hot line (i.e., Fe XXI) at the same footpoint location, largely due to the IRIS raster mode, for instance, the IRIS slit only scanned the edge of the footpoint location, where it was very weak and could not generate the hot (e.g., 10 MK) flare line. On the other hand, the mass converging motions driven by the chromospheric evaporation are also expected to be seen from double footpoints to the loop top along the new formed flare loop. Figure 2 shows that a hot flare loop in XRT Al_mesh, AIA 131 Å, and 94 Å connects double footpoints, which are overlayed on two ribbons in SJI 1400 Å, Hα line core, and AIA 1600 Å. The double footpoints rooted in the positive (Ft1) and negative (Ft2) polarities, respectively. They approach each other along the flare loop, merging together into one single source, as shown in Figure 2 (h). To study the mass motions in detail, we plot the time-distance diagrams along the hot flare loop in EUV images at a high temperature, such as AIA 131 Å, 94 Å, and 335 Å. Figure 6 presents the time-distance diagrams from 05:42:30 UT to 05:48:30 UT in these three wavebands. To clearly display the mass converging motions, the running difference rather than the original data series are used here. The converging mass motions can be obviously seen at wavelengths of AIA 131 Å, 94 Å, and 335 Å. They both move from double footpoints (Ft1 & Ft2) along the flare loop, merging together at the loop top (Lt), as indicated by the magenta arrows. During this process, the flare loop is filled up with hot plasmas. The converging motions are strongly indicative of upflows driven by the chromospheric evaporation. Interestingly, the onset time of the merging process at the loop top becomes later and later with the plasma temperature decreases, as indicated by the vertical dashed lines. For instance, the merging process starts at about 05:44:06 UT in AIA 131 Å (∼10 MK), and it becomes at around 05:44:30 UT in AIA 94 Å (∼6 MK), while it begins at about 05:44:38 UT in AIA 335 Å (∼3 MK). This is strongly related to the evaporation speeds of the converging flows, which can be estimated by the linear fitting. Then, the 3-sigma (3σ) uncertainty of the fitted parameter could be regarded as the error of the derived velocity. For example, the average evaporation speeds within error bars are estimated to be about 206±15 km s^{-1} and 210±16 km s^{-1} in AIA 131 Å. They decrease to roughly 153±9 km s^{-1} and 157±11 km s^{-1} in AIA 94 Å, and further decrease to around 126±5 km s^{-1} and 128±6 km s^{-1} in AIA 335 Å. This observational fact is consistent with previous findings, for instance, the temperature-dependent upflows for the coronal lines during the flare impulsive phase (e.g., Milligan & Dennis 2009; Chen & Ding 2010). Meanwhile, the converging mass motions takes place from ∼05:43:30 UT to ∼05:44:38 UT, which is after the C6.7 flare onset time and roughly equal to the lifetime (such as 1 minute) of the first HXR pulse recorded by the Fermi/GBM, as shown by the overplotted light curves. This implies that the upflows are strongly depending on the nonthermal energy.

The X-ray energy spectrum measured by the Fermi/GBM is used to analyze the deposited energy flux during the chromospheric evaporation, as shown in Figure 7. In this study, the two-components model such as a single thermal (vth) plus a non-thermal thick target (thick2) is used to fit the observed X-ray spectrum during the whole lifetime of the first HXR pulse, i.e., from

05:43:30 UT to 05:44:30 UT. Then, the cutoff energy (E_c) and the spectral index (γ) of the photon spectrum can be obtained from the fitting result. The Chi-squared residual (χ^2) shows a reasonable fitting result, i.e., $\chi^2 < 3$ (e.g., Sadykov et al. 2015). Thus, the nonthermal power (P) above the cutoff energy of the accelerated electrons could be estimated by using the Equation 1 (see, Aschwanden 2005; Zhang et al. 2016b).

$$P(E \geq E_c) = 1.16 \times 10^{24} \gamma^3 I_1 (\frac{E_c}{E_1})^{-(\gamma-1)}, \quad (1)$$

where I_1 represents the photon count rates at energies of $E \geq E_c$, and E_1 denotes the lower cutoff energy. Assuming that $I_1 \approx 10^3$ photon s^{-1} cm^{-2} for the C6.7 flare (Zhang et al. 2016b) and $E_c = E_1$ (Aschwanden 2005), $P(E \geq E_c)$ could be estimated to about 1.6×10^{29} erg s^{-1}. The X-ray source area (A) is estimated from the Hinode/XRT image, as outlined by the brown contour in Figure 1. Considering the projection effect, it is about 2.8×10^{18} cm^{-2}. So, the nonthermal energy flux (P/A) is roughly equal to $\sim5.7\times10^{10}$ erg s^{-1} cm^{-2}, which is large enough (i.e., $>10^{10}$ erg s^{-1} cm^{-2}) to drive the explosive evaporation (Fisher et al. 1985; Zarro et al. 1988; Kleint et al. 2016).

4. Conclusion and Discussion

Using the multi-wavelength observations measured by the NVST, IRIS, SDO/AIA, Fermi/GBM, Hinode/XRT, MUSER, and NoRP, we explored simultaneous observations of chromospheric evaporation and condensation in a C6.7 flare on 9 May 2019. The cool lines such as Si IV and C II measured by the IRIS show obviously red shifted velocities at slow speeds of about 15−19 km s^{-1} at one flare footpoint. The same red shifts can be seen in the LOS velocity image at double footpoints, which is derived from the two Hα off bands ($\pm$0.5 Å) observed by the NVST. Those red shifts at slow speeds in the solar chromosphere and transition region indicate the low-velocity downflows driven by the chromospheric condensation (e.g., Zhang et al. 2016a; Libbrecht et al. 2019; Yu et al. 2020). The high-temperature X-ray/EUV images detected by the Hinode/XRT and SDO/AIA show a hot flare loop, within double footpoints rooting in the positive and negative magnetic fields, respectively. The converging mass motions can be clearly seen from double footpoints to the loop top at fast speeds of 126−210 km s^{-1}, which could be the indicative of high-velocity upflows driven by the chromospheric evaporation (Li et al. 2017; Zhang et al. 2019). It should be pointed out that the estimated speeds from the time-distance diagram are horizontal components. On the other hand, the high-temperature EUV emissions in AIA 94 Å appear to rise from double footpoints to the loop top and eventually merge into a single source (see, Figure 2 h), which are quite similar to the converging motion of HXR sources (e.g., Liu et al. 2006, 2008; Ning et al. 2009; Ning 2011). Therefore, the motion velocities derived from the time-distance diagrams here are most possible to be the projected velocities of the upflows driven by the chromospheric evaporation rather than the motion of the flare loops. We would like to state that the C6.7 flare occurs closely to the solar disk center and the projection effect is quite weak. The low-velocity downflows of cool lines and the high-velocity upflows of hot plasmas are simultaneously observed during the impulsive phase

of the C6.7 flare, suggesting an explosive chromospheric evaporation (e.g., Milligan et al. 2006a; Tian et al. 2015; Zhang et al. 2016b; Brosius & Inglis 2017; Sadykov et al. 2019). Moreover, the nonthermal energy flux is estimated to be $\sim 5.7\times10^{10}$ erg s^{-1} cm^{-2}, implying a strong heating energy of the electron beams during the flare impulsive phase. Obviously, it is larger than the critical threshold between the gentle and explosive evaporations presented by Fisher et al. (1985). Meanwhile, the characteristic timescale of the chromospheric evaporation can be estimated from the converging mass motions of hot plasmas in Figure 6. It could also be estimated from the lifetime of the first HXR/microwave pulse in Figure 1. They both show a characteristic timescale of about 1 minute, which is equal to our previous finding (Li et al. 2018), and it is similar to the typical timescale of an explosive evaporation (Zarro et al. 1988; Liu et al. 2008; Sadykov et al. 2015). Our observational facts demonstrate an explosive chromospheric evaporation during the flare impulsive phase.

It is necessary to state that the physical origin of the explosive chromospheric evaporation. The IRIS observed the C6.7 flare in the raster mode rather than the fixed slit, and the time cadence of NVST is as low as about 43 s, while the HXR/micowave pulses only remains about 1 minute. We cannot obtain the point-to-point correspondence between the time series of Doppler velocities and HXR/micowave fluxes, as done in previous studies (Li et al. 2015; Tian et al. 2015; Li et al. 2018). We cannot find the spatial correlation between the upflows and HXR/micowave sources (see, Milligan & Dennis 2009; Brosius et al. 2016; Zhang et al. 2016b), because the lack of direct observation of HXR/micowave images. However, the explosive chromospheric evaporation occurred during the impulsive phase of the C6.7 flare, and the high-velocity upflows show a good temporal correlation with the evolution of the first HXR pulse observed by the Fermi/GBM, i.e, between ∼05:43:30 UT to ∼05:44:30 UT. The first HXR pulse corresponds well to the microwave pulse observed by the NoRP, which is also accompanied by a type III radio burst detected by the MUSER, as shown in Figure 1. Moreover, the heating energy released by electron beams is larger than the critical threshold (Fisher et al. 1985; Zarro et al. 1988; Sadykov et al. 2019). Therefore, the explosive chromospheric evaporation is most likely to be driven by nonthermal electrons accelerated by the magnetic reconnection during the flare impulsive phase (e.g., Tian et al. 2015; Warren et al. 2016; Zhang et al. 2016b; Li et al. 2017; Lee et al. 2017).

In this study, high-velocity upflows are identified as the fast evaporation speeds of the mass motions in AIA high-temperature EUV images. The evaporation speeds appear to be quite sensitive to the plasma temperature in the AIA EUV images. The AIA 131 Å emission during the solar flare is mainly emitted from the Fe XXI line, which has a formation temperature of about 10 MK (Lemen et al. 2012), and their evaporation speeds are estimated to be about 206−210 km s^{-1}. The AIA 94 Å radiation is from the Fe XVIII line with a formation temperature of roughly 6 MK (Lemen et al. 2012), and their evaporation speeds are about 153−157 km s^{-1}. The AIA 335 Å radiation is from the Fe XVI line with a formation temperature of roughly 3 MK (Lemen et al. 2012), and the evaporation speeds are around 126−128 km s^{-1}. Therefore, the hot plasmas originated from double footpoints in AIA 131 Å are first converging and merging at the loop-top region, while

those in AIA 335 Å are last converging and merging at the loop-top region in our observation, as indicated by the vertical dashed lines in Figure 6. Our observations are consistent with pervious findings using the spectroscopic observations (Milligan & Dennis 2009; Chen & Ding 2010). They found that the plasma velocities at flare footpoints strongly depend on the formation temperature of emission lines. However, we did not find the similar evaporation motions in the lower temperature EUV wavelengths, such as AIA 211 Å, 193 Å, and 171 Å. This is probably because that these AIA images are much easier to be saturated during the solar flare. Another possibility could be due to their lower response temperature. The evaporation motion may only appear at the higher temperature wavelengths, i.e., >2 MK (see, Milligan & Dennis 2009). It should be pointed out that there are two peaks (∼10 MK and ∼0.4 MK) in the profile of 131 Å temperature response function. Here, we chose the higher formation temperature (∼10 MK) as the AIA 131 Å response temperature, mainly because that the lower temperature EUV wavelengths (171 Å, 193 Å, and 211 Å) had very weak or even not response for the chromospheric evaporation in the C6.7 flare. In this study, we only investigate the explosive chromospheric evaporation during the first HXR/microwave pulse between roughly 05:43 UT and 05:45 UT. We also notice that the HXR/microwave fluxes show another two nonthermal pulses from about 05:45 UT to 05:49 UT, but we do not study them. This is because that the IRIS slit leaves the flare ribbon/footpoint, and the AIA EUV images are saturated when the flare reaches closely to its maximum.

We wanted to stress that the HXR source area is replaced by the X-ray source area (A) measured by the Hinode/XRT. This is due to the observational limitation, since the Fermi/GBM only provided the HXR flux during solar flares, we cannot find the HXR image for this flare. The X-ray source measured by the Hinode/XRT contains the hot loop seen in the AIA 131 Å, and it also includes two ribbons observed in the NVST Hα image, as shown in Figure 2. It should be larger than the HXR source. Therefore, the X-ray source area could be regarded as the upper limit of the HXR area, and it is indeed a bit larger than the previous finding for a C6.5-class flare (e,g., Zhang et al. 2016b). However, this does not affect our results, since the nonthermal energy flux is based on the minimum estimation, but it is still larger than the typical threshold of the explosive evaporation. On the other hand, it is well known that the spectral lines for Si IV and C II are optically thin and thick, respectively. Therefore, their Doppler velocities are determined by the different methods, for instance, the single Gaussian fitting for the Si IV lines, while the moment analysis technique for the C II lines (Li et al. 2019; Yu et al. 2020).

We would like to thank the anonymous referee for helping to improve the quality of the paper. We thank the teams of NVST, IRIS, SDO, MUSER, Fermi, Hinode/XRT, NoRP, and GOES for their open data use policy. This study is supported by NSFC under grant 11973092, 12073081, 11873095, 11790302, the Strategic Priority Research Program on Space Science, CAS, Grant No. XDA15052200 and XDA15320301. D. L. is also supported by the Surface Project of Jiangsu Province (BK20211402). The Laboratory No. 2010DP173032.

REFERENCES

Asai, A., Nakajima, H., Shimojo, M., et al. 2006, PASJ, 58, L1. doi:10.1093/pasj/58.1.L1

Aschwanden, M. J. & Benz, A. O. 1995, ApJ, 438, 997. doi:10.1086/175141

Aschwanden, M. J. 2005, Physics of the Solar Corona. An Introduction with Problems and Solutions (2nd edition), by M.J. Aschwanden. 892 pages. ISBN 3-540-30765-6, Library of Congress Control Number: 2005937065. Praxis Publishing Ltd., Chichester, UK; Springer, New York, Berlin, 2005.

Ashfield, W. H. & Longcope, D. W. 2021, ApJ, 912, 25. doi:10.3847/1538-4357/abedb4

Battaglia, M., Kleint, L., Krucker, S., et al. 2015, ApJ, 813, 113. doi:10.1088/0004-637X/813/2/113

Benz, A. O. 2017, Living Reviews in Solar Physics, 14, 2. doi:10.1007/s41116-016-0004-3

Brannon, S. R. 2016, ApJ, 833, 101. doi:10.3847/1538-4357/833/1/101

Brosius, J. W. & Holman, G. D. 2010, ApJ, 720, 1472. doi:10.1088/0004-637X/720/2/1472

Brosius, J. W. 2013, ApJ, 762, 133. doi:10.1088/0004-637X/762/2/133

Brosius, J. W. & Daw, A. N. 2015, ApJ, 810, 45. doi:10.1088/0004-637X/810/1/45

Brosius, J. W., Daw, A. N., & Inglis, A. R. 2016, ApJ, 830, 101. doi:10.3847/0004-637X/830/2/101

Brosius, J. W. & Inglis, A. R. 2017, ApJ, 848, 39. doi:10.3847/1538-4357/aa8a68

Brosius, J. W. & Inglis, A. R. 2018, ApJ, 867, 85. doi:10.3847/1538-4357/aae5f5

Carmichael, H. 1964, NASA Special Publication, 451

Chen, F. & Ding, M. D. 2010, ApJ, 724, 640. doi:10.1088/0004-637X/724/1/640

Chen, Y., Wu, Z., Liu, W., et al. 2017, ApJ, 843, 8. doi:10.3847/1538-4357/aa7462

Chen, B., Shen, C., Gary, D. E., et al. 2020, Nature Astronomy, 4, 1140. doi:10.1038/s41550-020-1147-7

Czaykowska, A., De Pontieu, B., Alexander, D., et al. 1999, ApJ, 521, L75. doi:10.1086/312176

Czaykowska, A., Alexander, D., & De Pontieu, B. 2001, ApJ, 552, 849. doi:10.1086/320553

De Pontieu, B., Title, A. M., Lemen, J. R., et al. 2014, Sol. Phys., 289, 2733. doi:10.1007/s11207-014-0485-y

De Pontieu, B., Polito, V., Hansteen, V., et al. 2021, Sol. Phys., 296, 84. doi:10.1007/s11207-021-01826-0

Ding, M. D., Watanabe, T., Shibata, K., et al. 1996, ApJ, 458, 391. doi:10.1086/176822

Dominique, M., Zhukov, A. N., Heinzel, P., et al. 2018, ApJ, 867, L24. doi:10.3847/2041-8213/aaeace

Doschek, G. A., Warren, H. P., & Young, P. R. 2013, ApJ, 767, 55. doi:10.1088/0004-637X/767/1/55

Dudík, J., Polito, V., Janvier, M., et al. 2016, ApJ, 823, 41. doi:10.3847/0004-637X/823/1/41

Falewicz, R., Rudawy, P., & Siarkowski, M. 2009, A&A, 508, 971. doi:10.1051/0004-6361/200912781

Fletcher, L. & Hudson, H. S. 2008, ApJ, 675, 1645. doi:10.1086/527044

Fletcher, L., Dennis, B. R., Hudson, H. S., et al. 2011, Space Sci. Rev., 159, 19. doi:10.1007/s11214-010-9701-8

Fisher, G. H., Canfield, R. C., & McClymont, A. N. 1985, ApJ, 289, 414. doi:10.1086/162901

Golub, L., Deluca, E., Austin, G., et al. 2007, Sol. Phys., 243, 63. doi:10.1007/s11207-007-0182-1

Graham, D. R. & Cauzzi, G. 2015, ApJ, 807, L22. doi:10.1088/2041-8205/807/2/L22

Graham, D. R., Cauzzi, G., Zangrilli, L., et al. 2020, ApJ, 895, 6. doi:10.3847/1538-4357/ab88ad

Hirayama, T. 1974, Sol. Phys., 34, 323. doi:10.1007/BF00153671

Hong, Z., Li, D., Zhang, M., et al. 2021, Sol. Phys., 296, 171. doi:10.1007/s11207-021-01922-1

Innes, D. E., Inhester, B., Axford, W. I., et al. 1997, Nature, 386, 811. doi:10.1038/386811a0

Jiang, C., Feng, X., Liu, R., et al. 2021, arXiv:2107.08204

Kamio, S., Kurokawa, H., Brooks, D. H., et al. 2005, ApJ, 625, 1027. doi:10.1086/429749

Karlicky, M. 1998, A&A, 338, 1084

Kleint, L., Heinzel, P., Judge, P., et al. 2016, ApJ, 816, 88. doi:10.3847/0004-637X/816/2/88

Kopp, R. A. & Pneuman, G. W. 1976, Sol. Phys., 50, 85. doi:10.1007/BF00206193

Krucker, S., Battaglia, M., Cargill, P. J., et al. 2008, A&A Rev., 16, 155. doi:10.1007/s00159-008-0014-9

Lee, K.-S., Imada, S., Watanabe, K., et al. 2017, ApJ, 836, 150. doi:10.3847/1538-4357/aa5b8b

Lemen, J. R., Title, A. M., Akin, D. J., et al. 2012, Sol. Phys., 275, 17. doi:10.1007/s11207-011-9776-8

Li, J. P. & Ding, M. D. 2004, ApJ, 606, 583. doi:10.1086/382860

Li, Y. & Ding, M. D. 2011, ApJ, 727, 98. doi:10.1088/0004-637X/727/2/98

Li, Y., Qiu, J., & Ding, M. D. 2012, ApJ, 758, 52. doi:10.1088/0004-637X/758/1/52

Li, D., Ning, Z. J., & Zhang, Q. M. 2015, ApJ, 813, 59. doi:10.1088/0004-637X/813/1/59

Li, L., Zhang, J., Peter, H., et al. 2016, Nature Physics, 12, 847. doi:10.1038/nphys3768

Li, D., Ning, Z. J., Huang, Y., et al. 2017, ApJ, 841, L9. doi:10.3847/2041-8213/aa71b0

Li, D., Li, Y., Su, W., et al. 2018, ApJ, 854, 26. doi:10.3847/1538-4357/aaa9c0

Li, Y., Ding, M. D., Hong, J., et al. 2019, ApJ, 879, 30. doi:10.3847/1538-4357/ab245a

Li, D. 2019, Research in Astronomy and Astrophysics, 19, 067. doi:10.1088/1674-4527/19/5/67

Li, D., Warmuth, A., Lu, L., et al. 2021, Research in Astronomy and Astrophysics, 21, 066. doi:10.1088/1674-4527/21/3/66

Libbrecht, T., de la Cruz Rodríguez, J., Danilovic, S., et al. 2019, A&A, 621, A35. doi:10.1051/0004-6361/201833610

Lin, J., Ko, Y.-K., Sui, L., et al. 2005, ApJ, 622, 1251. doi:10.1086/428110

Liu, W., Chen, Q., & Petrosian, V. 2013, ApJ, 767, 168. doi:10.1088/0004-637X/767/2/168

Liu, W., Liu, S., Jiang, Y. W., et al. 2006, ApJ, 649, 1124. doi:10.1086/506268

Liu, W., Petrosian, V., Dennis, B. R., et al. 2008, ApJ, 676, 704. doi:10.1086/527538

Liu, Z., Xu, J., Gu, B.-Z., et al. 2014, Research in Astronomy and Astrophysics, 14, 705-718. doi:10.1088/1674-4527/14/6/009

Lohmann, A. W., Weigelt, G., & Wirnitzer, B. 1983, Appl. Opt., 22, 4028. doi:10.1364/AO.22.004028

Loto'aniu, P., Rodriguez, J., Redmon, R., et al. 2017, EGU General Assembly Conference Abstracts

Lysenko, A. L., Frederiks, D. D., Fleishman, G. D., et al. 2020, Physics Uspekhi, 63, 818. doi:10.3367/UFNe.2019.06.038757

Mann, G. & Warmuth, A. 2011, A&A, 528, A104. doi:10.1051/0004-6361/201014389

Masuda, S., Kosugi, T., Hara, H., et al. 1994, Nature, 371, 495. doi:10.1038/371495a0

Meegan, C., Lichti, G., Bhat, P. N., et al. 2009, ApJ, 702, 791. doi:10.1088/0004-637X/702/1/791

Milligan, R. O., Gallagher, P. T., Mathioudakis, M., et al. 2006a, ApJ, 638, L117. doi:10.1086/500555

Milligan, R. O., Gallagher, P. T., Mathioudakis, M., et al. 2006b, ApJ, 642, L169. doi:10.1086/504592

Milligan, R. O. & Dennis, B. R. 2009, ApJ, 699, 968. doi:10.1088/0004-637X/699/2/968

Nakajima, H., Sekiguchi, H., Sawa, M., et al. 1985, PASJ, 37, 163

Ning, Z., Cao, W., Huang, J., et al. 2009, ApJ, 699, 15. doi:10.1088/0004-637X/699/1/15

Ning, Z. & Cao, W. 2010, ApJ, 717, 1232. doi:10.1088/0004-637X/717/2/1232

Ning, Z. & Cao, W. 2011, Sol. Phys., 269, 283. doi:10.1007/s11207-010-9693-2

Ning, Z. 2011, Sol. Phys., 273, 81. doi:10.1007/s11207-011-9833-3

Pesnell, W. D., Thompson, B. J., & Chamberlin, P. C. 2012, Sol. Phys., 275, 3. doi:10.1007/s11207-011-9841-3

Polito, V., Del Zanna, G., Valori, G., et al. 2017, A&A, 601, A39. doi:10.1051/0004-6361/201629703

Polito, V., Testa, P., Allred, J., et al. 2018, ApJ, 856, 178. doi:10.3847/1538-4357/aab49e

Priest, E. R. & Forbes, T. G. 2002, A&A Rev., 10, 313. doi:10.1007/s001590100013

Raftery, C. L., Gallagher, P. T., Milligan, R. O., et al. 2009, A&A, 494, 1127. doi:10.1051/0004-6361:200810437

Reep, J. W., Bradshaw, S. J., & Alexander, D. 2015, ApJ, 808, 177. doi:10.1088/0004-637X/808/2/177

Reep, J. W. & Russell, A. J. B. 2016, ApJ, 818, L20. doi:10.3847/2041-8205/818/1/L20

Rubio da Costa, F., Liu, W., Petrosian, V., et al. 2015, ApJ, 813, 133. doi:10.1088/0004-637X/813/2/133

Sadykov, V. M., Vargas Dominguez, S., Kosovichev, A. G., et al. 2015, ApJ, 805, 167. doi:10.1088/0004-637X/805/2/167

Sadykov, V. M., Kosovichev, A. G., Sharykin, I. N., et al. 2019, ApJ, 871, 2. doi:10.3847/1538-4357/aaf6b0

Schou, J., Scherrer, P. H., Bush, R. I., et al. 2012, Sol. Phys., 275, 229. doi:10.1007/s11207-011-9842-2

Shibata, K. & Magara, T. 2011, Living Reviews in Solar Physics, 8, 6. doi:10.12942/lrsp-2011-6

Sturrock, P. A. & Coppi, B. 1964, Nature, 204, 61. doi:10.1038/204061a0

Sturrock, P. A. 1966, Nature, 211, 695. doi:10.1038/211695a0

Song, Y. L., Guo, Y., Tian, H., et al. 2018, ApJ, 854, 64. doi:10.3847/1538-4357/aaa7f1

Su, Y., Veronig, A. M., Holman, G. D., et al. 2013, Nature Physics, 9, 489. doi:10.1038/nphys2675

Sui, L. & Holman, G. D. 2003, ApJ, 596, L251. doi:10.1086/379343

Tan, B.-L., Yan, Y., Li, T., et al. 2020, Research in Astronomy and Astrophysics, 20, 090. doi:10.1088/1674-4527/20/6/90

Temmer, M., Veronig, A. M., Vršnak, B., et al. 2007, ApJ, 654, 665. doi:10.1086/509634

Teriaca, L., Falchi, A., Cauzzi, G., et al. 2003, ApJ, 588, 596. doi:10.1086/373946

Tian, H., Li, G., Reeves, K. K., et al. 2014, ApJ, 797, L14. doi:10.1088/2041-8205/797/2/L14

Tian, H., Young, P. R., Reeves, K. K., et al. 2015, ApJ, 811, 139. doi:10.1088/0004-637X/811/2/139

Tian, H. & Chen, N.-H. 2018, ApJ, 856, 34. doi:10.3847/1538-4357/aab15a

Veronig, A. M., Rybák, J., Gömöry, P., et al. 2010, ApJ, 719, 655. doi:10.1088/0004-637X/719/1/655

Warren, H. P., Reep, J. W., Crump, N. A., et al. 2016, ApJ, 829, 35. doi:10.3847/0004-637X/829/1/35

Warmuth, A. & Mann, G. 2020, A&A, 644, A172. doi:10.1051/0004-6361/202039529

Weigelt, G. P. 1977, Optics Communications, 21, 55. doi:10.1016/0030-4018(77)90077-3

Woods, T. N., Caspi, A., Chamberlin, P. C., et al. 2017, ApJ, 835, 122. doi:10.3847/1538-4357/835/2/122

Xiang, Y.-. yuan ., Liu, Z., & Jin, Z.-. yu . 2016, New A, 49, 8. doi:10.1016/j.newast.2016.05.002

Yan, X. L., Yang, L. H., Xue, Z. K., et al. 2018a, ApJ, 853, L18. doi:10.3847/2041-8213/aaa6c2

Yan, X. L., Wang, J. C., Pan, G. M., et al. 2018b, ApJ, 856, 79. doi:10.3847/1538-4357/aab153

Yan, X., Liu, Z., Zhang, J., et al. 2020a, Science in China E: Technological Sciences, 63, 1656. doi:10.1007/s11431-019-1463-6

Yan, X., Xue, Z., Cheng, X., et al. 2020b, ApJ, 889, 106. doi:10.3847/1538-4357/ab61f3

Yan, X., Wang, J., Guo, Q., et al. 2021a, ApJ, 919, 34. doi:10.3847/1538-4357/ac116d

Yan, Y., Zhang, J., Wang, W., et al. 2009, Earth Moon and Planets, 104, 97. doi:10.1007/s11038-008-9254-y

Yan, Y., Chen, Z., Wang, W., et al. 2021b, Frontiers in Astronomy and Space Sciences, 8, 20. doi:10.3389/fspas.2021.584043

Young, P. R., Tian, H., & Jaeggli, S. 2015, ApJ, 799, 218. doi:10.1088/0004-637X/799/2/218

Yu, K., Li, Y., Ding, M. D., et al. 2020, ApJ, 896, 154. doi:10.3847/1538-4357/ab9014

Zarro, D. M., Canfield, R. C., Strong, K. T., et al. 1988, ApJ, 324, 582. doi:10.1086/165919

Zhang, Q. M., Li, D., & Ning, Z. J. 2016a, ApJ, 832, 65. doi:10.3847/0004-637X/832/1/65

Zhang, Q. M., Li, D., Ning, Z. J., et al. 2016b, ApJ, 827, 27. doi:10.3847/0004-637X/827/1/27

Zhang, Q. M., Li, D., & Huang, Y. 2019, ApJ, 870, 109. doi:10.3847/1538-4357/aaf4b7

This preprint was prepared with the AAS LaTeX macros v5.2.

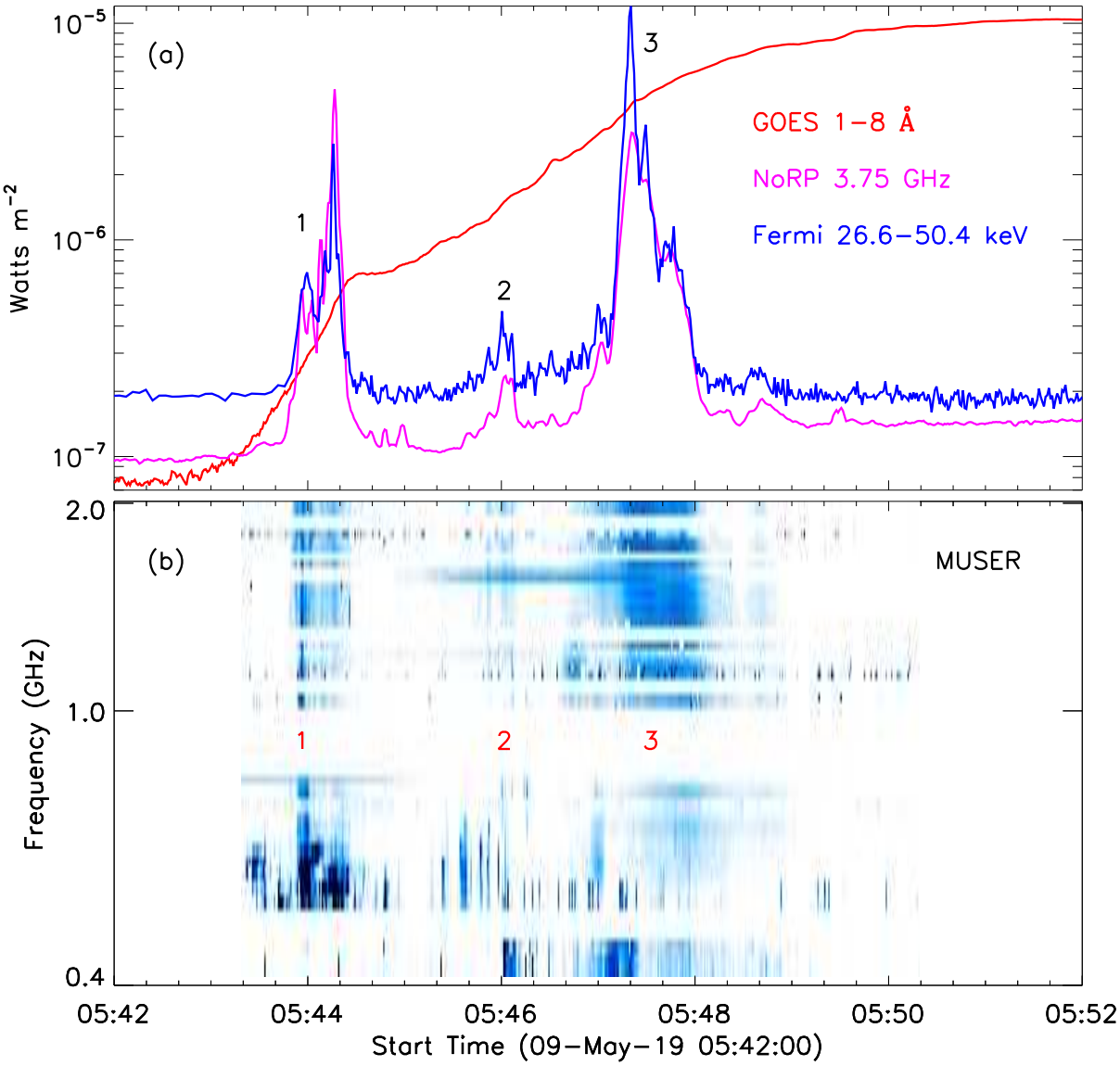

Fig. 1.— Overview of the solar flare on 9 May 2019. Panel (a): Full-disk light curves from 05:42 UT to 05:52 UT, recorded by the GOES 1−8 Å (red), NoRP 3.75 GHz (magenta), and Fermi 26.6−50.4 keV (blue), respectively. Panel (b): The radio dynamic spectrum observed by the MUSER. The Roman numerals mark three nonthermal pulses.

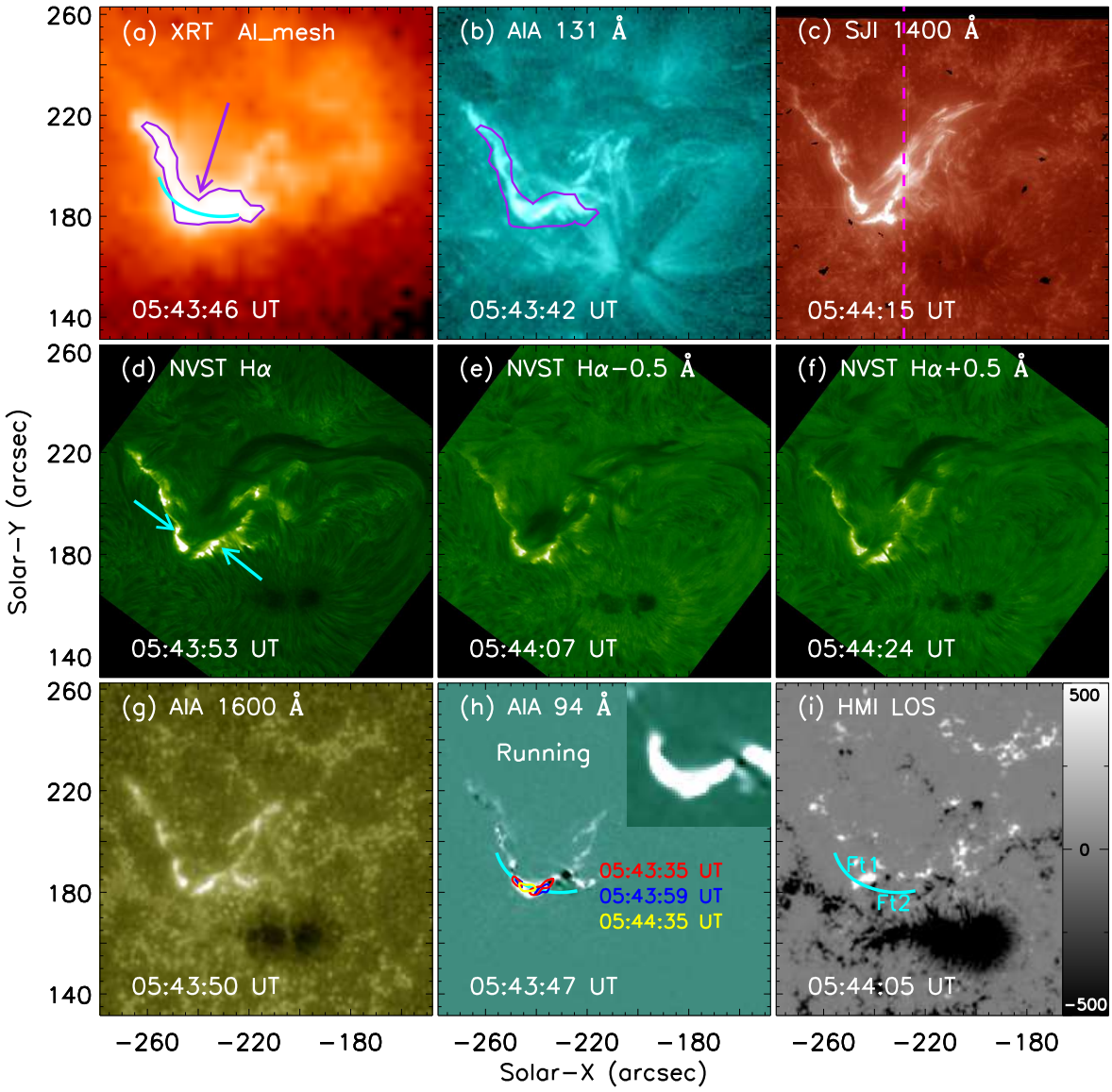

Fig. 2.— Multi-wavelength snapshots with a FOV of about 130″×130″ of the C6.7 flare observed by the Hinode/XRT (a), IRIS/SJI (c), the NVST (d−f), SDO/AIA (b, g, h), and SDO/HMI (i). The purple profile is made from the XRT image, and the contour level is set at 80% of the maximum intensity. The purple arrow indicates the flare loop, and two cyan arrows mark flare ribbons. The vertical magenta line represents the IRIS slit. Panel (h) presents the running difference map, and the overplotted contours are EUV emissions in AIA 94 Å at the level of 60% at three fixed instances of time. The zoomed image shows the AIA 94 Å running difference map with a small FOV of about 30″×30″. The cyan curve marks the flare loop used to perform the time-distance diagrams in Figure 6.

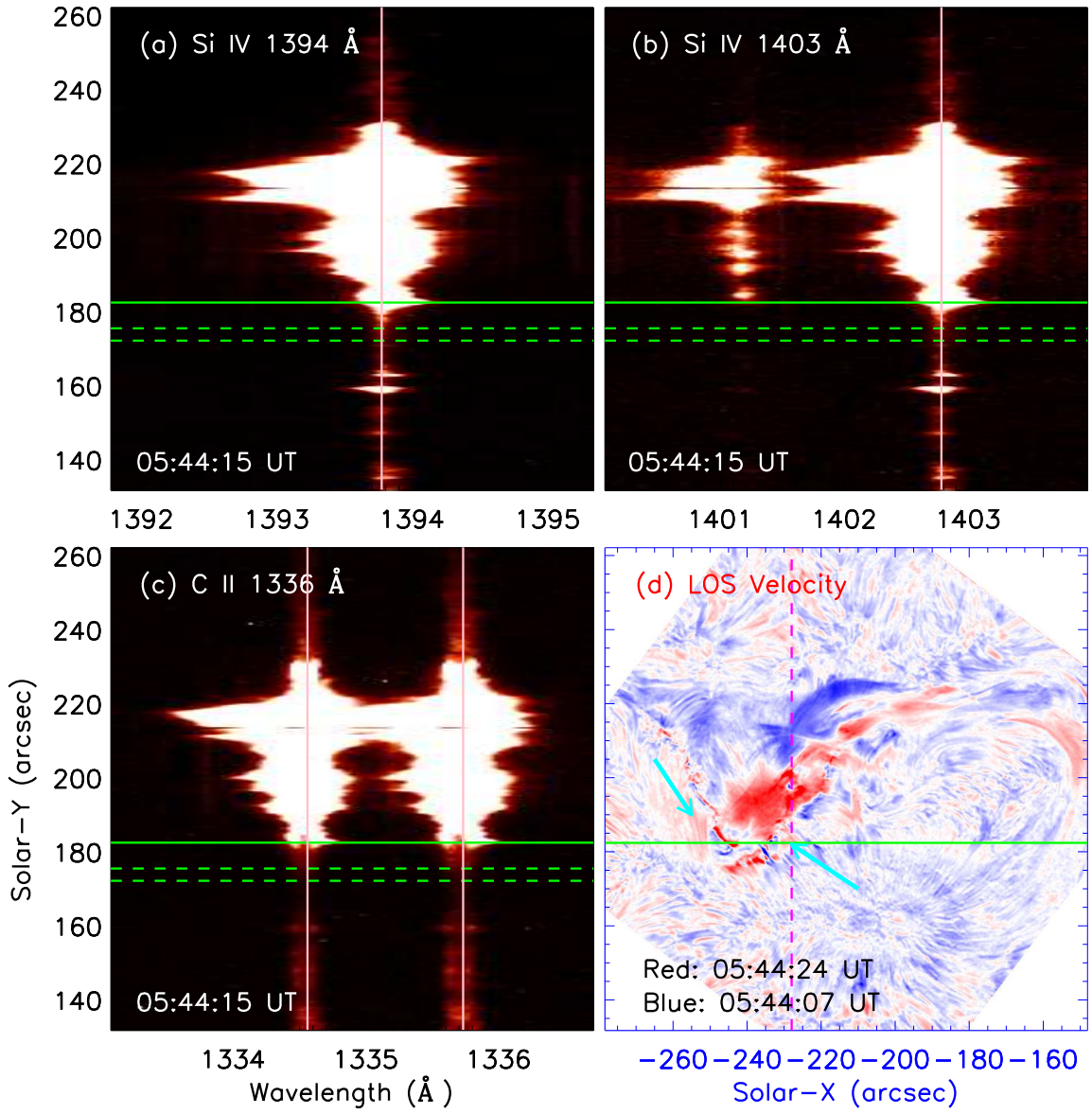

Fig. 3.— Panels (a)−(c): IRIS spectra at three FUV windows of 'Si IV 1394 Å' (a), 'Si IV 1403 Å' (b), and 'C II 1336 Å' (c). The horizontal lines mark the flare footpoint location (solid) and quiet region (dashed). The vertical pink lines mark the positions of the reference line centers. Panel (d): LOS velocity image derived from two Hα off bands at $\pm$0.5 Å, measured by the NVST. The vertical magenta line represents the IRIS slit, and the cyan arrows indicated two flare footpoints.

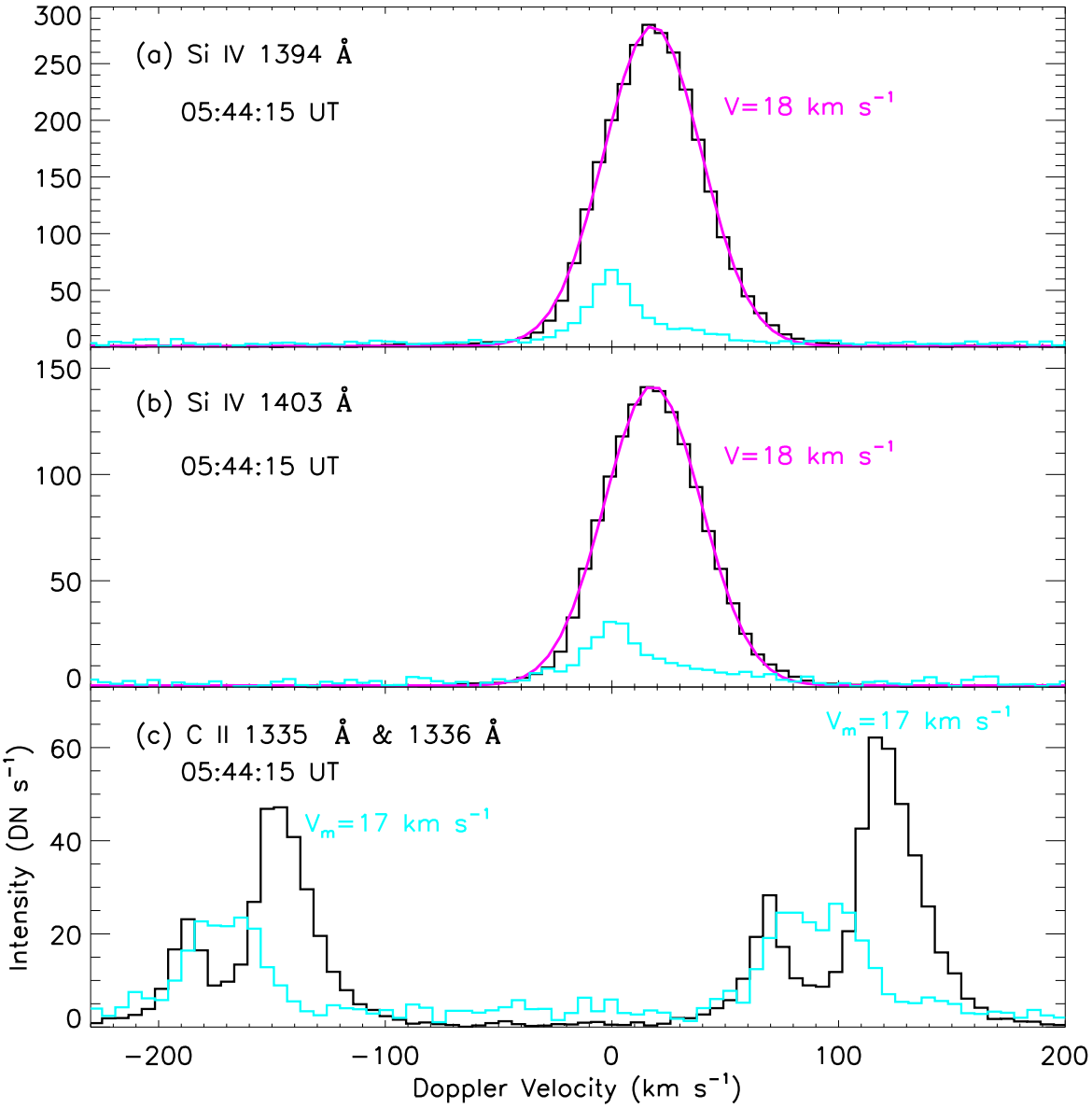

Fig. 4.— Line spectra at the flare footpoint location (black) and quiet region (cyan, after multiplying by 10) at ∼05:44:15 UT. The magenta curves represent the single Gaussian fitting results. The Doppler velocities of the Si IV and C II lines are also given.

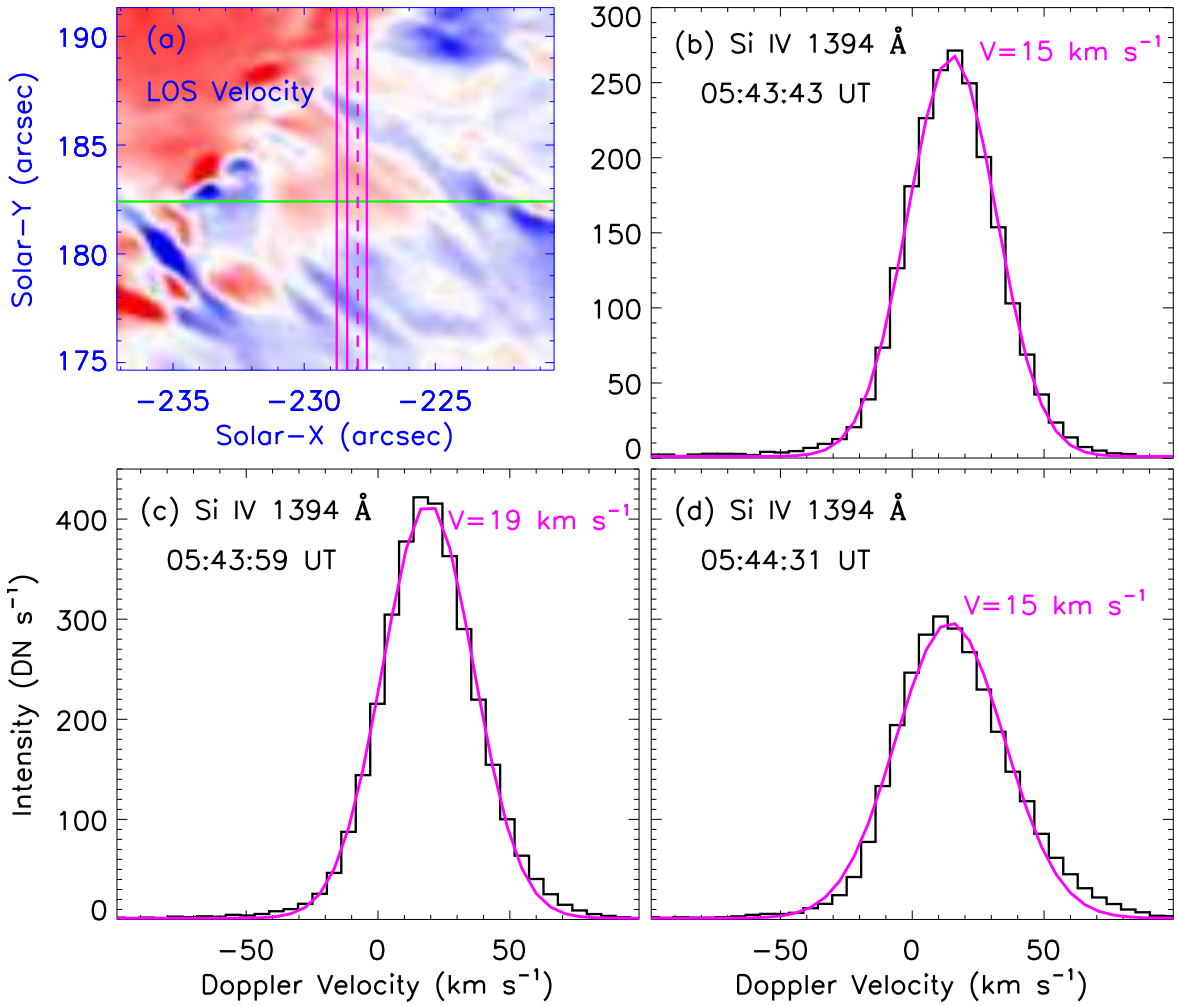

Fig. 5.— Panel (a): Same as Figure 3 (d) but with a small FOV of ∼16.5″×16.5″ observed by the NVST. The vertical magenta lines mark IRIS slits. Panels(b)−(d): Line spectra for Si IV 1394 Å (black) and their single Gaussian fitting results (magenta) at three different slits, as marked by the vertical solid lines in panel (a). The Doppler velocities are also given.

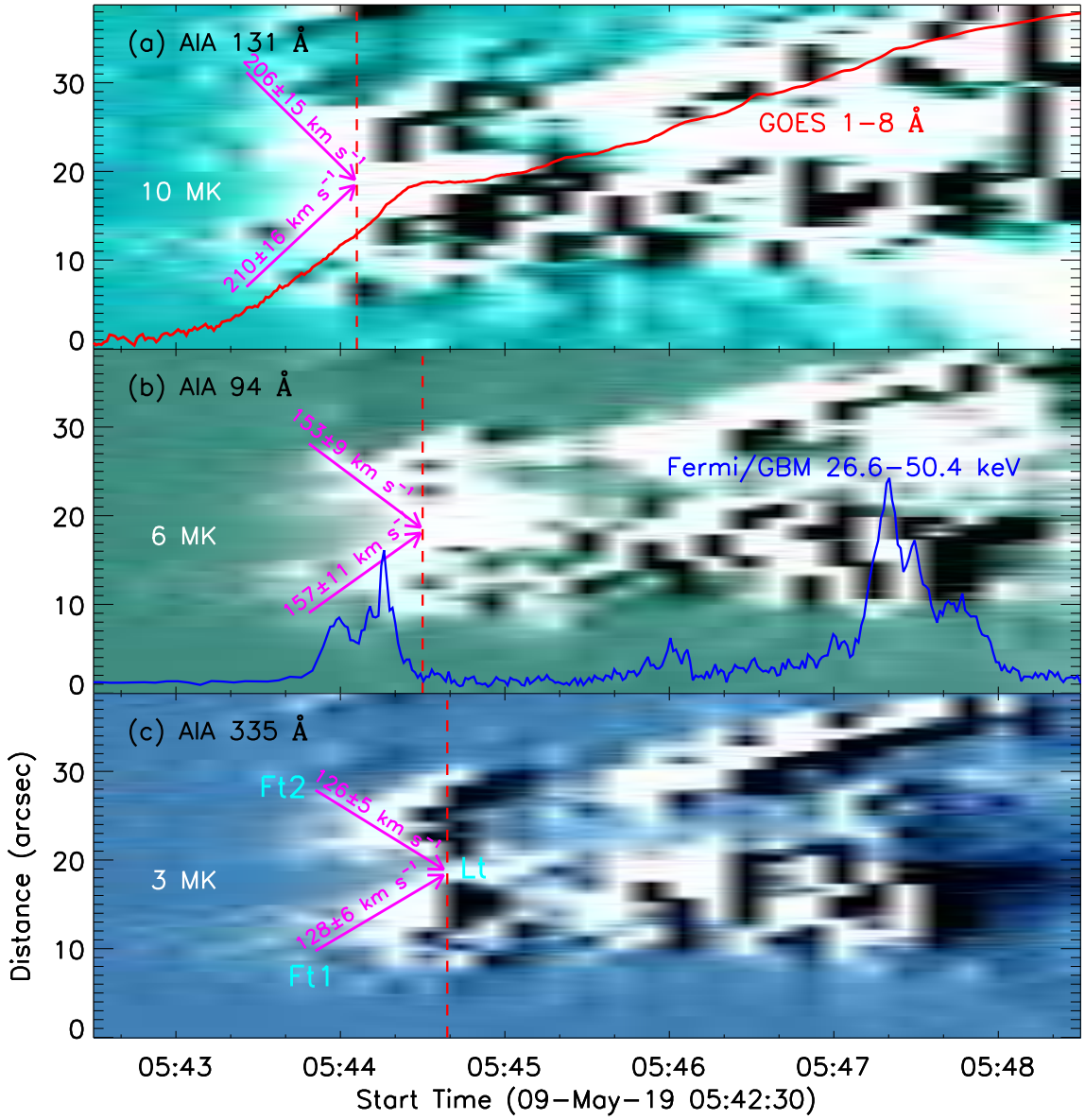

Fig. 6.— Time-distance diagrams along the flare loop, made from the AIA data series in 131 Å (a), 94 Å (b), and 335 Å (c), respectively. The magenta arrows indicate the upflows from double footpoints (Ft), and the vertical dashed lines mark the onset time of merging processes at the loop-top (Lt) region. The overplotted line curves are the GOES 1–8 Å (red) and Fermi 26.6–50.4 keV (blue) fluxes.

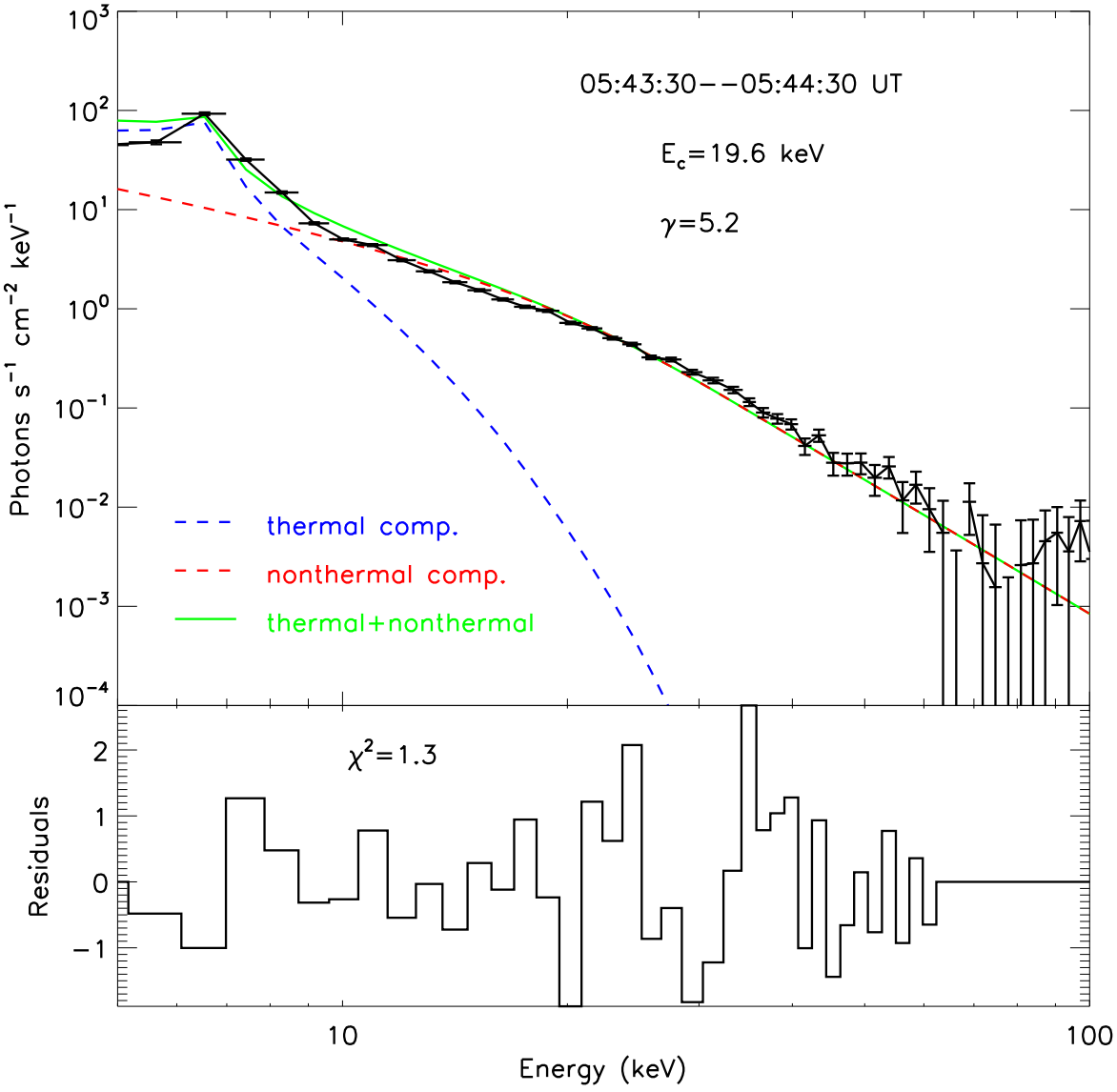

Fig. 7.— Fermi/GBM X-ray spectrum with an integrated time of 1 minute during 05:43:30−05:44:30 UT, the fitted thermal (blue) and nonthermal (red) components, as well as the sum of both components (green). The low-energy cutoff (E_c), spectral index (γ), and the Chi-squared residual (χ^2) are labeled.

Table 1: Details of observational instruments used in this paper.

Instruments	Wavebands	Cadence	Pixel scale	Descriptions
IRIS	1394 & 1403 Å	∼16.2 s	∼0.33″	Si IV lines
	1335 & 1336 Å	∼16.2 s	∼0.33″	C II lines
	SJI 1400 Å	∼65 s	∼0.33″	FUV image
NVST	6562.8 Å	∼43 s	∼0.165″	Hα line core
	±0.5 Å	∼43 s	∼0.165″	Hα off bands
SDO	AIA 94, 131 & 335 Å	12 s	0.6″	EUV image
	AIA 1600 Å	24 s	0.6″	UV image
	HMI LOS	45 s	0.6″	Magnetogram
Hinode/XRT	Al_mesh	–	∼4.1″	X-ray image
GOES-16	1−8 Å	1 s	-	SXR flux
Fermi/GBM	26.6−50.4 keV	∼4.096 s	-	HXR flux
	5−100 keV	∼4.096 s	-	X-ray spectrum
MUSER	0.4−2 GHz	0.025 s	-	Radio dynamic spectrum
NoRP	3.75 GHz	1 s	-	Microwave flux